Available online at www.sciencedirect.com

SciVerse ScienceDirect

Ceramics International 39 (2013) 3809–3816

CERAMICS INTERNATIONAL

www.elsevier.com/locate/ceramint

Phase transformation on hydroxyapatite decomposition

Shih-Fu Ou[a,b,c], Shi-Yung Chiou[b], Keng-Liang Ou[a,c,d,*]

[a]Research Center for Biomedical Devices and Prototyping Production, Taipei Medical University, Taipei 110, Taiwan
[b]Institute of Mold & Die Engineering, National Kaohsiung University of Applied Sciences, Kaohsiung 807, Taiwan
[c]Graduate Institute of Biomedical Materials and Tissue Engineering, Taipei Medical University, Taipei 110, Taiwan
[d]Research Center for Biomedical Implants and Microsurgery Devices, Taipei Medical University, Taipei 110, Taiwan

Received 12 October 2012; received in revised form 13 October 2012; accepted 17 October 2012
Available online 26 October 2012

Abstract

The collapse of sintered hydroxyapatite (HA) has been attributed to HA decomposition; however, the detailed variations in microstructure are still unclear. Two phase transformation routes of HA decomposition during sintering were identified by transmission electron microscopy in this study. In the first route, HA is transformed to tetracalcium phosphate and needle-like β-tricalcium phosphate which is subsequently converted to α-tricalcium phosphate (α-TCP) above 1100 °C. In the second route, HA is transformed directly to α-TCP and calcium oxide at 1400 °C, accompanied by nanopore formation. In the second route, the α-TCP grew with a preferred orientation to form stripe-like grains. Further holding at 1400 °C for 4 h resulted in recrystallization; i.e., equi-axial grains formed within a stripe-like grain. Nanopore defects dispersed in the α-TCP grains are the main factor for the low density and decreased mechanical strength of the sintered bulk.

Keywords: B. Electron microscopy; C. Diffusion; D. Apatite; E. Biomedical applications

1. Introduction

Hydroxyapatite (HA) is one of the most attractive bioceramics for replacing human hard tissue and is considered to be bioactive and nonbiodegradable [1–4] because of its closed resemblance to bones and teeth [5]. The well-known HA phase transformation during sintering consists of two processes: dehydroxylation and decomposition. In dehydroxylation, HA gradually loses OH ions at elevated temperature and turns to oxyhydroxyapatite (OHA) [6,7] as shown in Eq. (1).

$$Ca_{10}(PO_4)_6(OH)_2 \rightarrow Ca_{10}(PO_4)_6(OH)_{2-2x}O_x\square_x + xH_2O \quad (1)$$

In this, an original hydroxyl site is replaced by an oxygen and a vacancy; consequently, OHA forms, and the symmetry is distorted. The dehydroxylation comprises three stages overall [8]: at low temperature (< 800 °C), reversible dehydroxylation proceeds at a slow rate. At an intermediate temperature (800–1350 °C), reversible dehydroxylation is accompanied by HA decomposition, i.e., HA can decompose into α-calcium phosphate (α-TCP), β-calcium phosphate (β-TCP) and calcium phosphate (CaO) according to the reaction in Eq. (2) [9].

$$Ca_{10}(PO_4)_6(OH)_2 \rightarrow 2Ca_3(PO_4)_2 + Ca_3(P_2O_8) + CaO + H_2O \quad (2)$$

Wang et al.[10] have studied how sintering of HA is affected by dehydroxylation as well as decomposition and concluded that preventing OH ions loss can effectively suppress decomposition. Furthermore, Ruy et al. [8] indicated that HA decomposition caused defects appeared on the bulk surface as observed by scanning electron microscopy (SEM). However, these surface defects have a microscale size, revealing that they are not the direct products of decomposition but occurred only when the inner channels were closed. Therefore, thorough investigation of defects' origin is necessary. This study attempts to understand the detailed mechanism of HA

*Corresponding author at: Taipei Medical University, Research Center for Biomedical Devices and Prototyping Production, Taipei 110, Taipei, Taiwan. Tel.: +886 2 27361661x5100; fax: +886 2 27395524.
E-mail address: klou@tmu.edu.tw (K.-L. Ou).

0272-8842/$ - see front matter © 2012 Elsevier Ltd and Techna Group S.r.l. All rights reserved.
http://dx.doi.org/10.1016/j.ceramint.2012.10.221

decomposition by using a powerful tool, transmission electron microscopy (TEM).

2. Experimental procedure

2.1. Sample compaction and sintering

A commercially available stoichiometric HA powder (Merck, Germany) was used in this study. The HA powder was compressed at 300 MPa, and the press was maintained for 1 min, yielding green compacts with a diameter of 10 mm and a thickness of 1.25 mm. These compacts were sintered in air at 1100, 1200, and 1300 °C at a ramp rate of 5 °C/min using a heating furnace and soaked for 1 h then cooled at a rate of 5 °C/min. To study the phase variation at high temperatures, the green compacts were further heated at 1400 °C and held for 1, 2, 3, and 4 h in air.

2.2. Characteristics of sintered compacts

The hardness of the HA compacts was measured by a Vickers hardness tester (MVK-H1, Meter-Mitutoyo, Japan)). After the sample surfaces were polished, indentations were performed on them at a testing load of 300 N for an indentation time of 15 s. Archimedes' method was used to evaluate the density of the sintered compacts. Six samples were examined for each sintering parameter in order to obtain an average relative density and hardness.

The compositions of the sintered compacts were characterized by powder X-ray diffractometry (XRD) (Model 2200, Rigaku Co., Tokyo, Japan). Monochromatic Cu Kα radiation was used for excitation under operating conditions of 40 kV and 30 mA. The XRD data were collected over a 2θ range of 20–45° at a step size of 0.04°/step and a count time of 5 s.

The microstructure of the sintered compacts was examined using SEM (SEM; Model JSM, JEOL Co., Tokyo, Japan). TEM (TEM; Model JEM2100, JEOL Co., Tokyo, Japan) observations were used to characterize the unknown phases. Specimens for TEM observation were mounted to 3 mm copper grids, mechanically thinned and Ar-ion-beam milled.

3. Results and discussion

3.1. Morphology

The as-received HA powder, shown in Fig. 1(a), consisted of small and large aggregates of irregular shape with an average particle size of approximately 18.7 μm. The aggregates composing fine columnar HA crystals was shown in upper right corner (Fig. 1(a)) which were held together by liquid capillary forces or electrostatic and van der Waals forces.

When the sintered compact was sintered at 1100 °C, local interconnections between grains via necks were observed, in addition, large cavities were still present as shown in Fig. 1(b). Fig. 1(c) shows a denser structure after sintered at 1200 °C and the average grain size (~1.68 μm) was slightly larger than that of the compact sintered at 1100 °C (~1.29 μm). As Fig. 1(d) shows, at 1300 °C, the grains became interconnected by thick, strong necks and the average grain size was approximately 3.38 μm. After 1 h at 1400 °C (Fig. 1(e)), nearly spherical aggregates formed, and the cavities were mostly closed. When the compact was held at 1400 °C for 3 h (Fig. 1(f)), narrow stripe-like crystals were observed locally on the grains. After 4 h at 1400 °C, crystals with wider stripes were frequently observed; the striped crystals consisting of several small crystals were also observed (Fig. 1(g), upper right).

3.2. XRD analysis

Fig. 2 shows the XRD patterns of the as-received HA and compacts sintered at various temperatures. The first products of HA decomposition, the β-TCP and tetracalcium phosphate (TTCP) phases, appeared at 1100 °C, as described in Eq. (3), which agrees well with the results reported by others [11,12]. Although the equilibrium phase diagram of the $CaO–P_2O_5$ system [13–15] indicates that CaO appears at 1720 °C. Sung's study showed that CaO can form when sintering a starting material with a Ca/P ratio greater than 1.7 at 1000 °C [12]. Consequently, CaO is expected to form as the temperature increases because HA is transformed to β-TCP and TTCP, accompanied by a non-uniform distribution of Ca and P; therefore, some areas may contain a high Ca/P ratio.

With a further increase in temperature to 1200 °C, the peak at 31.07° gradually shifted to 30.75° and was identified as α-TCP, revealing a gradual transformation of the trigonal β-TCP phase into monoclinic α-TCP at 1125 °C, and then, above 1189 °C, an accelerated transition of β-TCP to α-TCP occurs [13,16,17]. In Suvorova's [18] recent study, not only α-TCP but also the CaO phase were detected by heating β-TCP at 1200 °C, as described in Eq. (4), but the amount of CaO was very small, approximately 0.095 times that of α-TCP [18]. Hence, in this study, the XRD patterns suggest that CaO formation started at 1100–1200 °C, although the CaO peak is too weak to be distinguishable until 1300 °C.

At sintering temperatures higher than 1300 °C, various crystal planes of α-TCP and CaO appeared in the XRD pattern, suggesting that another phase transformation route is proceeding. Fig. 4(c) shows that the interface of HA and α-TCP indicates the transformation of HA to α-TCP in the compact sintered at 1400 °C for 1 h. The XRD and TEM results together demonstrated that HA is transformed directly to α-TCP and CaO, which is in accordance with Eq. (5). It is reasonable that CaO crystals were not discovered by TEM observations even though several CaO peaks appeared in the XRD patterns because TEM observations were localized, and a previous study

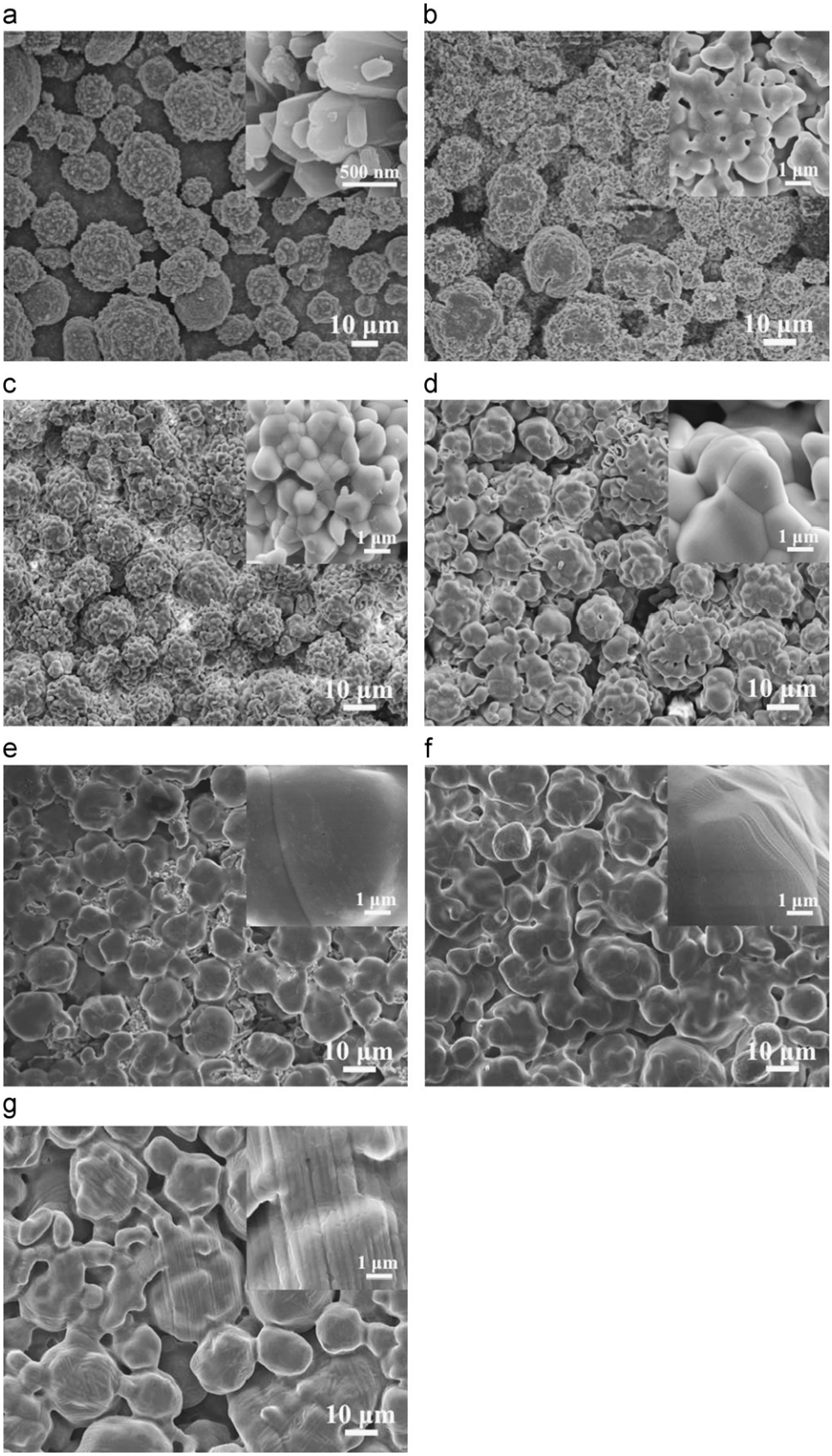

Fig. 1. SEM micrographs of (a) HA powder and HA compacts sintered at (b) 1100 °C, (c) 1200 °C, (d) 1300 °C for 1 h. (e), (f) and (g) HA compact sintered at 1400 °C for 1, 3 and 4 h, respectively.

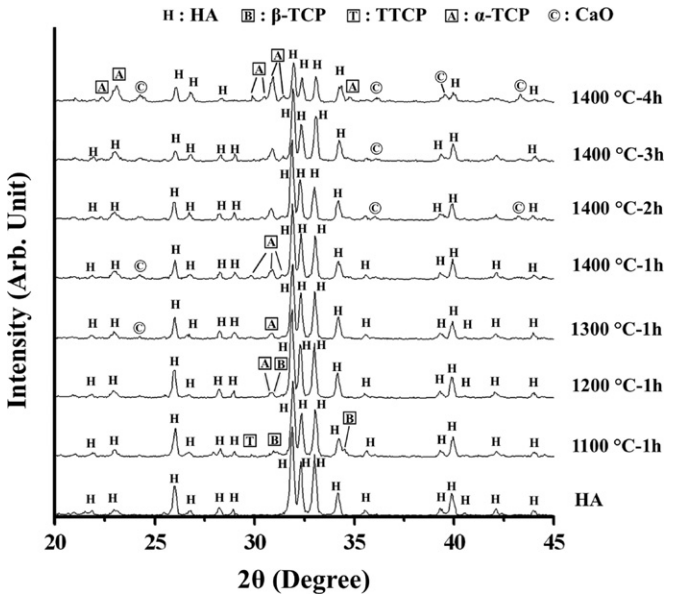

Fig. 2. XRD patterns of HA powder and HA compacts sintered at 1100 °C, 1200 °C, 1300 °C for 1 h and at 1400 °C for 1, 2, 3 and 4 h.

has demonstrated that decomposition occurred only in certain parts of the bulk material [18].

$$Ca_{10}(PO_4)_6OH_2 \rightarrow 3\ \beta\text{-}Ca_3(PO_4)_2 + Ca_4P_2O_9 + H_2O \quad (3)$$

$$3\ \beta\text{-}Ca_3(PO_4)_2 \rightarrow 3\ \alpha\text{-}Ca_3(PO_4)_2 + CaO \quad (4)$$

$$Ca_{10}(PO_4)_6\ OH_2 \rightarrow 3\ \alpha\text{-}Ca_3(PO_4)_2 + CaO + H_2O \quad (5)$$

The relative amounts of various phases in the sintered compact were calculated as follows [19]:

$$P_1/P_1^0 = w_1M_1/w_1(M_1 - M_2) + M_2$$

P_1^0 and P_1 are the integrated intensity of selected reflection from the pure material and the sintered sample, respectively, and w_1 is the weight fraction of phase 1. The mass absorption coefficients of α-TCP and HA, denoted as M_1 and M_2, are 97.08 and 87.38, respectively. The calculated ratio of α-TCP in the sintered compact is shown in Fig. 8.

3.3. TEM observation

Fig. 3(a) shows the HA compact sintered at 1100 °C. A crystal with dark contrast (labeled as 1) underneath blade-like crystals (indicated by arrows) was observed. The selected area diffraction pattern (SAPD) indicated that the crystal at 1 is an HA grain with the [−1 1 −1] zone axis. Fig. 3(b), a highly magnified view of Fig. 3(a), shows the blade-like crystals that formed from the grain boundary of HA grains and the SADP taken from the blade-like crystals revealed they are β-TCP structure.

Fig. 4(a) shows the TEM micrographs of HA compacts sintered at 1400 °C for 1 h. A triple pocket was observed, and the SADP of the grain (labeled as 2) was identified as a single HA grain. Fig. 4(b) is a highly magnified view of Fig. 4(a); the SADP exhibits an HA pattern in the grain (labeled as 3) with the [01-1] zone axis. Fig. 4(c) shows a

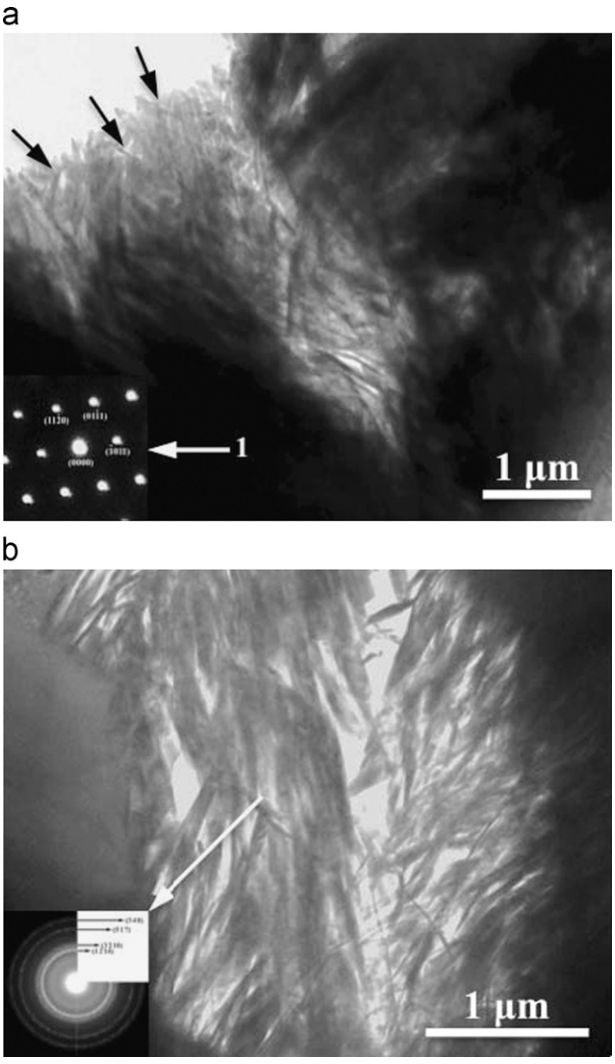

Fig. 3. (a) TEM micrographs of HA compact sintered at 1100 °C. (b) The high magnified view of (a).

high resolution TEM (HRTEM) image of the selected area (dashed square) in Fig. 4(b). A solid area (left side) and a pore-containing area (right side) were observed; the interface is marked by a dashed line. Filtered HRTEM images taken from the solid area and the pore-containing area associated with HA and α-TCP, respectively, are also shown in Fig. 4(c). The α-TCP crystals exhibited two major orientations of the grains, which appear in the simulated HRTEM image in the upper left part of Fig. 4(c). Furthermore, the observed pores approximately 10 nm in size, which we called nanopores were attributed to water loss resulting from HA decomposition.

Fig. 5 shows the TEM micrographs of HA sintered at 1400 °C for 4 h. Fig. 5(a) shows a typical grain junction; one grain along the [0 2 1] zone axis was identified as HA structure by the SADP. In addition, stripe-like crystals (Fig. 5(b)) with different aspect ratios were also observed. Fig. 5(c), a highly magnified image of Fig. 5(b), shows that these striped crystals contained numerous pores of different sizes, indicating that the striped crystals were porous.

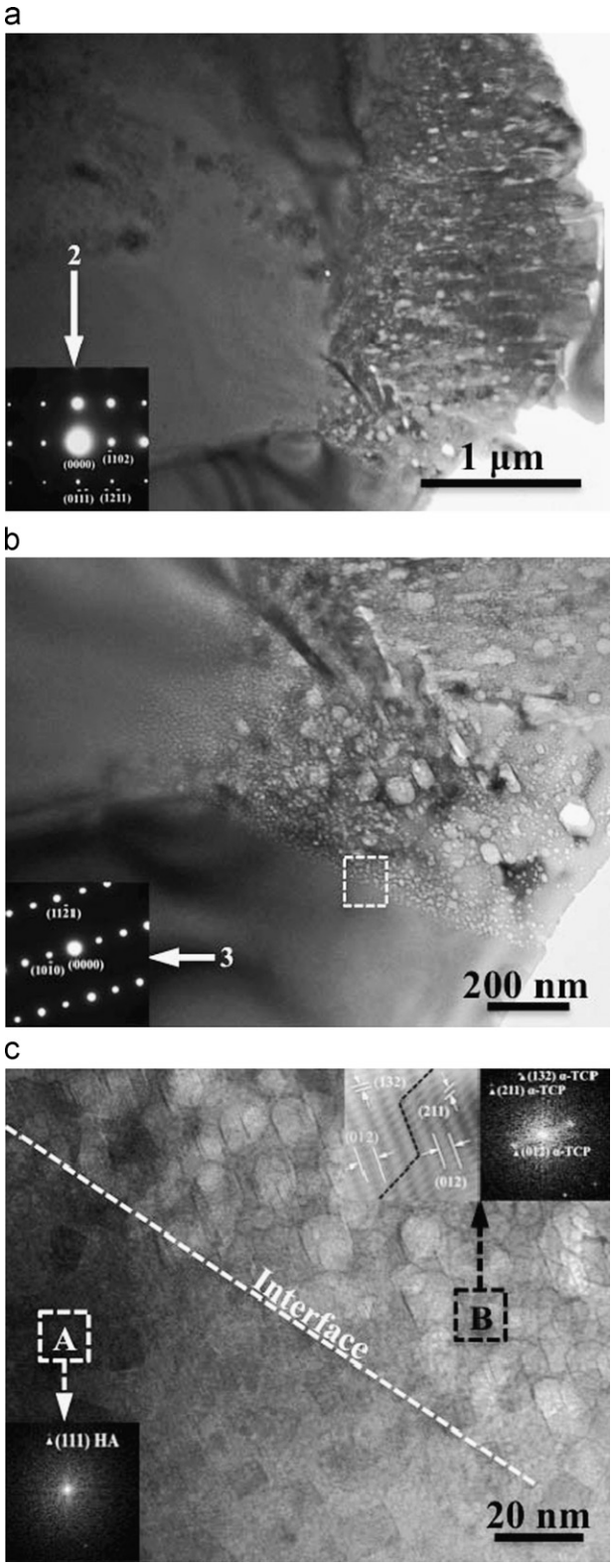

Fig. 4. (a) TEM micrographs of HA compact sintered at 1400 °C for 1 h. (b) The high magnified view of (a) and (c) HRTEM micrograph of (b).

HRTEM was performed on a single grain of the striped crystal and a FET was used to obtain the crystalline orientation. The lattice fringe corresponding to (0 1 2) is broadly distributed in Fig. 5(d), but other lattice fringes related to (16-2), (13-3), (0 4 3), and (0 3 1) appear locally. Fig. 5(d) also shows that individual nanocrystals grew in close contact, and the lattice plane images were resolved well enough to identify them as α-TCP. Fig. 5(e) shows a SEM micrograph of the compact sintered at 1400 °C for 4 h, (a highly magnified view of Fig. 1(g)); it indicates that the striped crystal was some 500 nm in width and was composed of many small equi-axis grains. However, these equi-axis grains (Fig. 5(e)) were relatively larger than the nanocrystals observed in Fig. 5(d) when comparing Fig. 5(d) and (e). Consequently, the nanocrystals were considered to be the recrystallized grains that nucleated within α-TCP (0 1 2) matrix and were expected to grow to isolated grains, as shown in Fig. 5(e).

3.4. Densification studies

Fig. 6 shows the effect of sintering temperature on the grain size and relative density of the sintered compacts. The relative density of the compact increased gradually to a maximum of 87% and reached a plateau at 1350 °C. However, at 1400 °C, a further increase in duration caused a decrease in the density. Densification is a process of eliminating the pores along the grain boundaries that were introduced during green compact fabrication. During the initial sintering, grain boundaries moved faster than pores, so isolated pores remained within the grain interior. Although pores could be moved by surface diffusion, this is hard to achieve [20], so the maximum density was limited; when the compact was sintered at high temperature, the density usually decreased, which was attributed to HA decomposition. This phenomenon is discussed later in this paper.

In addition, with regard to grain growth, the grain size variation with temperature can be divided into two temperature regions. At relatively low temperature (1100–1350 °C), grains grew slowly from an average size of 1.3–5.4 μm; then, between 1350 and 1400 °C, they grew at an accelerated rate to 8.3 μm. With a further increase in the sintering duration, the grains continued to grow. As mentioned above, at low temperature, the pores remaining along the grain boundaries impeded grain growth. Retardation of grain boundaries migration by pores [21] usually occurred at a relative density of 0.65–0.9%. In contrast, when the open pores collapsed to form isolated pores within grains, the extent to which pores pinned grain boundaries decreased, accelerating grain growth.

The activation energy for grain growth was also calculated by establishing an Arrhenius plot (Fig. 7) according to relationship between grain size and temperature. The slope of the line in the Fig. 7 was used to determine the activation energy (Q) from the following equation by using:

$$D = A\exp\ (Q/RT)$$

where T is the temperature, D is the average grain size, and R is the gas constant (8.314 kJ/kmol K). In this study, the

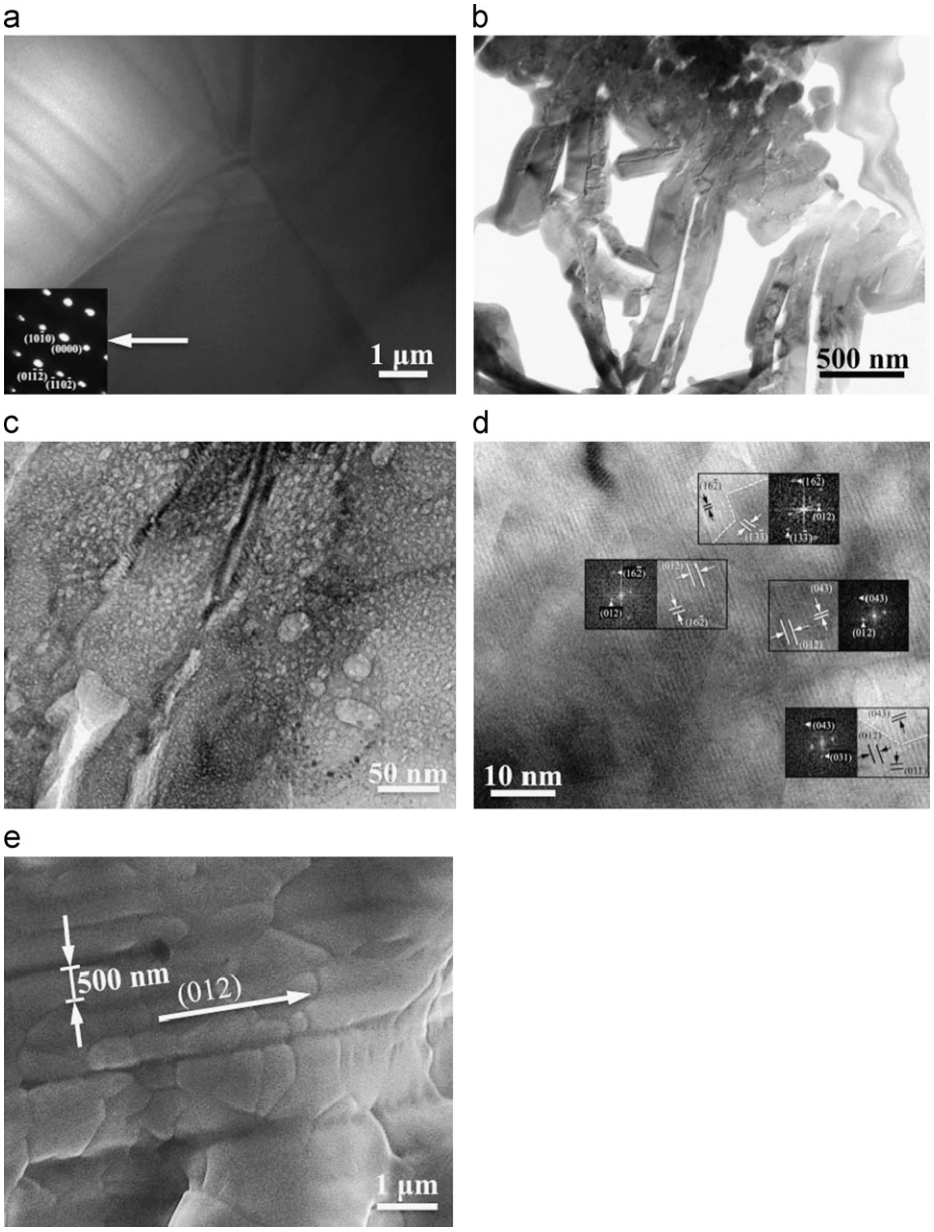

Fig. 5. (a) and (b) are TEM micrographs of HA compact sintered at 1400 °C for 4 h. (c) The high magnified view of (b). (d) HRTEM micrograph of (c). (e) SEM micrographs of HA compact sintered at 1400 °C for 4 h.

activation energy for grain growth in HA is approximately 54 kcal/mol, which corresponded to the values associated with apatite sintering that were provided by other researchers, i.e., 47 kcal/mol [22], 56 kcal/mol [19], 57 kcal/mol [23], and 58 kcal/mol [11].

3.5. Hardness tests

Fig. 8 shows the hardness of sintered compacts as a function of sintering temperature. The hardness increased as the temperature increased to a maximum hardness of 5.52 GPa at 1350 °C and followed by the first decrement as the temperature increased to 1400 °C. After further holding temperature at 1400 °C, a second decrease in hardness occurred after 2 h of soaking time, and a significantly higher number of hardness values were distributed at the lower limit. On the other hand, Fig. 8 also shows the ratio of α-TCP in the sintered compact as a function of sintering temperature, which was calculated on the basis of the XRD patterns. This amount of α-TCP increased greatly after the compact was sintered at 1400 °C for 2 h.

The mechanical properties of sintered compact generally varied with the sintering temperature and depended on the density, grain size and phase composition. The hardness and relative density as functions of grain size are shown in Fig. 9. When the grain size was less than 5.5 μm, the hardness of the sintered compact increased as the density increased at relatively low temperatures. At grain size

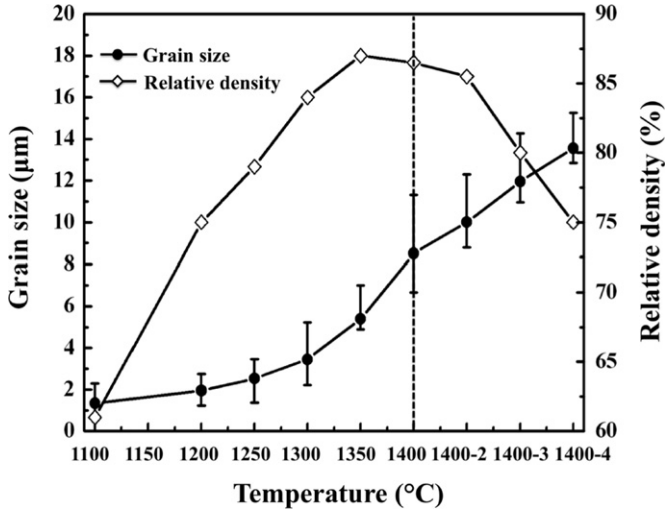

Fig. 6. Variation of grain size and relative density as a function of sintering temperature.

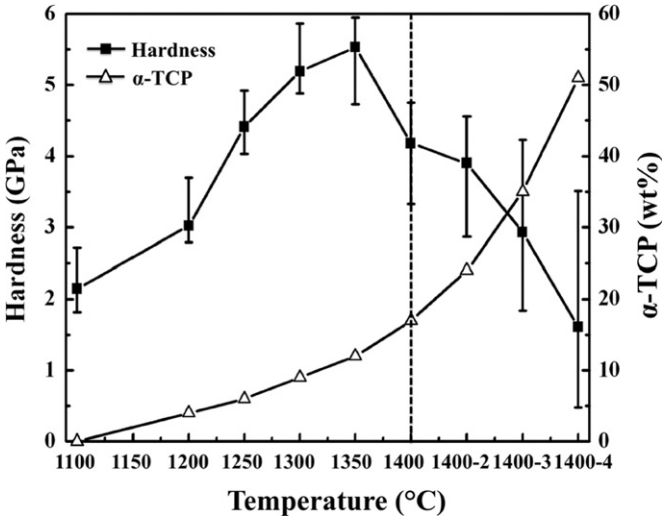

Fig. 8. Variation of hardness and amount of α-TCP as a function of sintering temperature.

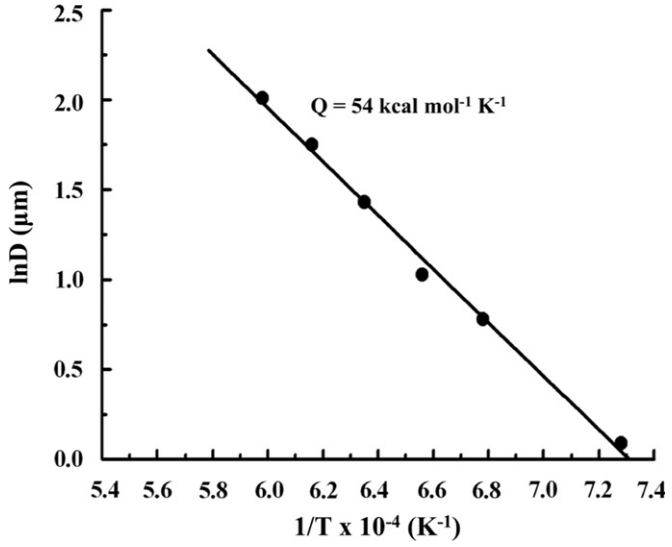

Fig. 7. Log average grain size versus reciprocal of sintering temperature of HA.

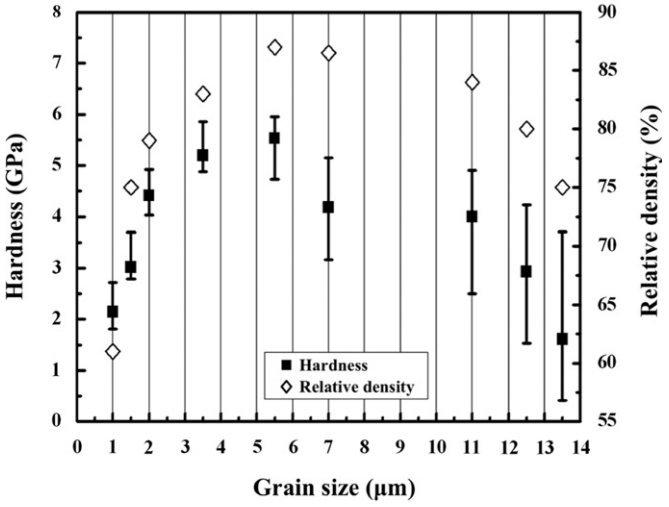

Fig. 9. Variation of hardness and relative density as a function of average grain size.

greater than 5.5 μm, the hardness exhibited a different trend from the density; i.e. a decline in hardness occurred, but no significant change in density appeared. Hence, this hardness decline was attributed to grain growth over the critical size, which was approximately 5.5 μm, in this study. Afterwards, after sintering at 1400 °C for 2 h, a secondary decrease in both hardness and density occurred. Therefore, an additional factor was considered to affect hardness and density. Many studies have investigated the relationship between grain size and mechanical properties including hardness [9–11,24], fracture toughness [8,9,19,24] and bending strength [9]. However, fewer papers mentioned the way that HA decomposition affects mechanical properties in terms of microstructure.

In the TEM micrographs (Fig. 4), α-TCP that formed within the HA matrix possessed many nanopore defects. This loose structure was considered the main factor causing not only a deterioration in mechanical strength but also a decrease in the density of the compact. A significantly lower number of hardness values are distributed in the lower limit in Fig. 8 after sintering of the compacts at 1400 °C for 3 and 4 h, which demonstrates that the areas containing α-TCP are relatively weak areas of the compact. In brief, the variation in hardness during sintering comprises three stages. First, at 1100–1350 °C, the hardness increased as a result of densification. After 1350 °C, grains grew to the critical grain size; there were fewer grain boundaries and lower hardness. Finally, at 1400 °C for 2 h, both grain growth and dramatic HA decomposition affected the hardness; however, the former was gradually replaced by the latter, which become the predominant factor with increasing temperature or sintering duration.

4. Conclusions

This study investigated the influence of sintering temperature on the densification and mechanical properties of HA compacts in terms of their microstructure. From 1100 to 1350 °C, a thermal activation process caused the sintered bulk to densify and strengthen; in contrast, after holding at 1400 °C, a considerable structural deterioration, identified by decreased density and hardness, appeared. Evaluation of the microstructure revealed two phase transformation routes of HA decomposition during sintering. At relatively low temperatures, HA transformed to TTCP and needle-like β-TCP, which was subsequently converted to α-TCP and CaO above 1100 °C. In this period, the phase transformation has less effect on the properties of the sintered bulk. At 1400 °C, in the second route, HA was transformed directly to α-TCP and CaO, and nanopores formed. After the sintering period at 1400 °C was further extended, equi-axial α-TCP grains grew within striped grains. In addition, nanopores existed only within the α-TCP and surrounded the interface of α-TCP–HA interface but did not in the HA matrix. Increasing the temperature to above the critical temperature caused rapid increases in the amounts of α-TCP and the number of nanopores, which severely degraded the density and strength of the sintered bulk.

Acknowledgments

The authors would like to thank the Center of Excellence for Clinical Trial and Research in Neurology and Neurosurgery, Taipei Medical University-Wan Fang Hospital, for financially supporting this research under contract No. DOH 101-TD-B-111-003.

References

[1] M. Jarcho, Calcium phosphate ceramics as hard tissue prosthesis, Clinical Orthopaedics and Related Research 157 (1981) 259–278.
[2] R.Z. LeGeros, Calcium phosphate materials in restorative dentistry: a review, Advances in Dental Research 2 (1988) 164–180.
[3] K. de Groot, Bioceramics consisting of calcium phosphate salts, Biomaterials 1 (1980) 47–50.
[4] K.-L. Ou, J. Wu, W.-T. Lai, C.-B. Yang, W.-C. Lo, L.-H. Chiu, Effects of the nanostructure and nanoporosity on bioactive nanohydroxyapatite/reconstituted collagen by electrodeposition, Journal of Biomedical Materials Research Part A 92A (2010) 906–912.
[5] L.L. Hench, Bioceramics, Journal of the American Ceramic Society 81 (1998) 1705–1728.
[6] A. Krajewski, A. Ravaglioli, L.R. di Sanseverino, F. Marchetti, G. Monticelli, The behaviour of apatite-based ceramics in relation to the critical 1150–1250 °C temperature range, Biomaterials 5 (1984) 105–108.
[7] T. Kijima, M. Tsutsumi, Preparation and thermal properties of dense polycrystalline oxyhydroxyapatite, Journal of the American Ceramic Society 62 (1979) 455–460.
[8] A.J. Ruys, M. Wei, C.C. Sorrell, M.R. Dickson, A. Brandwood, B.K. Milthorpe, Sintering effects on the strength of hydroxyapatite, Biomaterials 16 (1995) 409–415.
[9] C.K. Wang, C.P. Ju, J.H. Lin, Effect of doped bioactive glass on structure and properties of sintered hydroxyapatite, Materials Chemistry and Physics 53 (1998) 138–149.
[10] P.E. Wang, T.K. Chaki, Sintering behaviour and mechanical properties of hydroxyapatite and dicalcium phosphate, Journal of Materials Science: Materials in Medicine 4 (1993) 150–158.
[11] G. Muralithran, S. Ramesh, The effects of sintering temperature on the properties of hydroxyapatite, Ceramics International 26 (2000) 221–230.
[12] Y.-M. Sung, J.-C. Lee, J.-W. Yang, Crystallization and sintering characteristics of chemically precipitated hydroxyapatite nanopowder, Journal of Crystal. Growth 262 (2004) 467–472.
[13] R.W. Nurse, J.H. Welch, W. Gutt, A new form of tricalcium phosphate, Nature 182 (1958) 1230–1231.
[14] J.H. Welch, W. Gutt, High-temperature studies of the system calcium oxide-phosphorus pentoxide, Journal of the Chemical Society 44 (1961) 42–44.
[15] E.R. Kreidler, F.A. Hummel, Phase relationships in the system SrO-P_2O_5 and the influence of water vapor on the formation of $Sr_4P_2O_9$, Inorganic Chemistry 6 (1967) 884–891.
[16] B. Dickens, L.W. Schroeder, W.E. Brown, Crystallographic studies of the role of Mg as a stabilizing impurity in β-$Ca_3(PO_4)_2$, The crystal structure of pure β-$Ca_3(PO_4)_2$, Journal of Solid State Chemistry 10 (1974) 232–248.
[17] M. Mathew, L.W. Schroeder, B. Dickens, W.E. Brown, The crystal structure of [alpha]-$Ca_3(PO_4)_2$, Acta Crystallographica Section B 33 (1977) 1325–1333.
[18] E.I. Suvorova, N.A. Arkharova, P.A. Buffat, Transmission electron microscopy of Ca oxide nano- and microcrystals in α-tricalcium phosphate prepared by sintering of β-tricalcium phosphate, Micron 40 (2009) 563–570.
[19] M. Jarcho, C. Bolen, M. Thomas, J. Bobick, J. Kay, R. Doremus, Hydroxylapatite synthesis and characterization in dense polycrystalline form, Journal of Materials Science 11 (1976) 2027-1035.
[20] B. Kellett, F.F. Lange, Stresses induced by differential sintering in powder compacts, Journal of the American Ceramic Society 67 (1984) 369–371.
[21] R.J. Brook, Pores and grain growth kinetics, Journal of the American Ceramic Society 52 (1969) 339–340.
[22] P. Van Landuyt, F. Li, J.P. Keustermans, J.M. Streydio, F. Delannay, E. Munting, The influence of high sintering temperatures on the mechanical properties of hydroxylapatite, Journal of Materials Science: Materials in Medicine 6 (1995) 8–13.
[23] K. Kamiya, T. Yoko, K. Tanaka, Y. Fujiyama, Growth of fibrous hydroxyapatite in the gel system, Journal of Materials Science 24 (1989) 827–832.
[24] N. Thangamani, K. Chinnakali, F.D. Gnanam, The effect of powder processing on densification, microstructure and mechanical properties of hydroxyapatite, Ceramics International 28 (2002) 355–362.